Chapter 5

Velocity fields in red supergiant stars

Contents

5.1 The tomography technique

Velocity fields in stellar atmospheres can be deduced from the study of line profiles. However, studies of individual line profiles require a resolving power of at least 10^5 and a high S/N ($\sim$ 100) (see Dravins 1982). Unfortunately, strong molecular bands veil the optical spectra of RSGs and they hamper these studies in the optical.
An alternative method is the tomography technique developed by Alvarez et al. (2001). The basic idea is to design a set of numerical templates, or "masks" (series of hole placed at the selected line position) that probe different optical depths. The high resolution spectra are cross-correlated with these masks and the resulting cross-correlation functions (CCF) may be seen as an average profile of the lines belonging to a typical formation depth. This technique takes advantage of the ability of the cross-correlation method to reveal complex profile despite the severe crowding of the optical spectra.
The tomography method relies on the ability to construct reliable synthetic spectra of late-type stars and to select the right set of spectral lines forming at a given depth. For this purpose, Alvarez et al. computed synthetic spectra from static models of red giant stars in spherical symmetry (MARCS models, Gustafsson et al. 1975, Plez et al. 1992 and Gustafsson et al. 2008) in the range $3850 - 6900$ Å. The masks are built from these spectra as in Fig. 5.1, where only 3 Å are represented. In this Figure, x is the reference optical depth ($\lg \tau_0$) at which $\tau_\lambda = 2/3$. In the Eddington-Barbier approximation, the

emerging flux $F_\lambda = S_\lambda\,(\tau_\lambda = 2/3)$. Masks (x_{min}, x_{max}) are constructed by punching holes at the position of lines that reach $x_{min} \leq x\,(\tau_\lambda = 2/3) < x_{max}$.

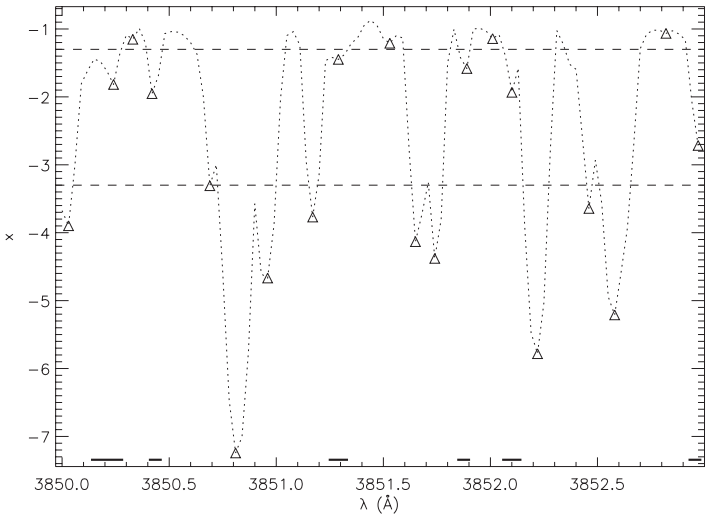

Figure 5.1: The synthetic masks (thick dashed ticks at the bottom of the plot) selects the lines forming in the region at depth $-1.3 \leq x < -3.3$ (dashed lines). The triangles denote the local minima of the depth function x (they correspond to the spectral line): when a local minima falls into the range scanned, a hole is created in the template. Figure from Alvarez et al. (2001).

Alvarez et al. found that when these templates, constructed with the complete set of lines, were applied to non-variable stars, spurious secondary peaks appeared in the CCF obtained with some masks. This was due to the fact that there were some errors in the line position of molecular lines (especially TiO). Thus, they decided to consider only the more accurate atomic lines for building the templates.
In this work, eight masks have been used, designated C1 to C8 (the same as Alvarez et al.), respectively, probing the innermost (faint lines, with excitation potential of $\chi_{exc} \sim 3$ eV) to the outermost layers (strong lines, $\chi_{exc} \sim 1$ eV). The CCF are symmetric for an hydrostatic, spherically-symmetric star and they will be shifted to the radial velocity of the star. Nevertheless, if a peculiar velocity field (shock wave propagating or expanding atmosphere) is present, the symmetry in the CCF is broken.
Josselin & Plez (2007) used these masks to derive CCF from time series spectroscopic observations of a sample of RSG and Fig. 5.2 shows two typical example. The CCFs present a wide variety of shapes for each star and from one mask to another for the same star. The innermost mask, C1, is systematically blueshifted compared to outer layers (C5 to C8). Moreover, the asymmetry in the CCF increases as one progresses from the inner to the outer layers. The mask C8 (the outermost layer) has a complex profile, with line doubling most of the time; on the other side, C1 mostly has a symmetric profile. C8 masks show systematically, where the two components are found, one blueshifted component and one redshifted with respect to the innermost layers. Josselin & Plez observed temporal variability of the depth, central velocity and asymmetries of the CCFs.

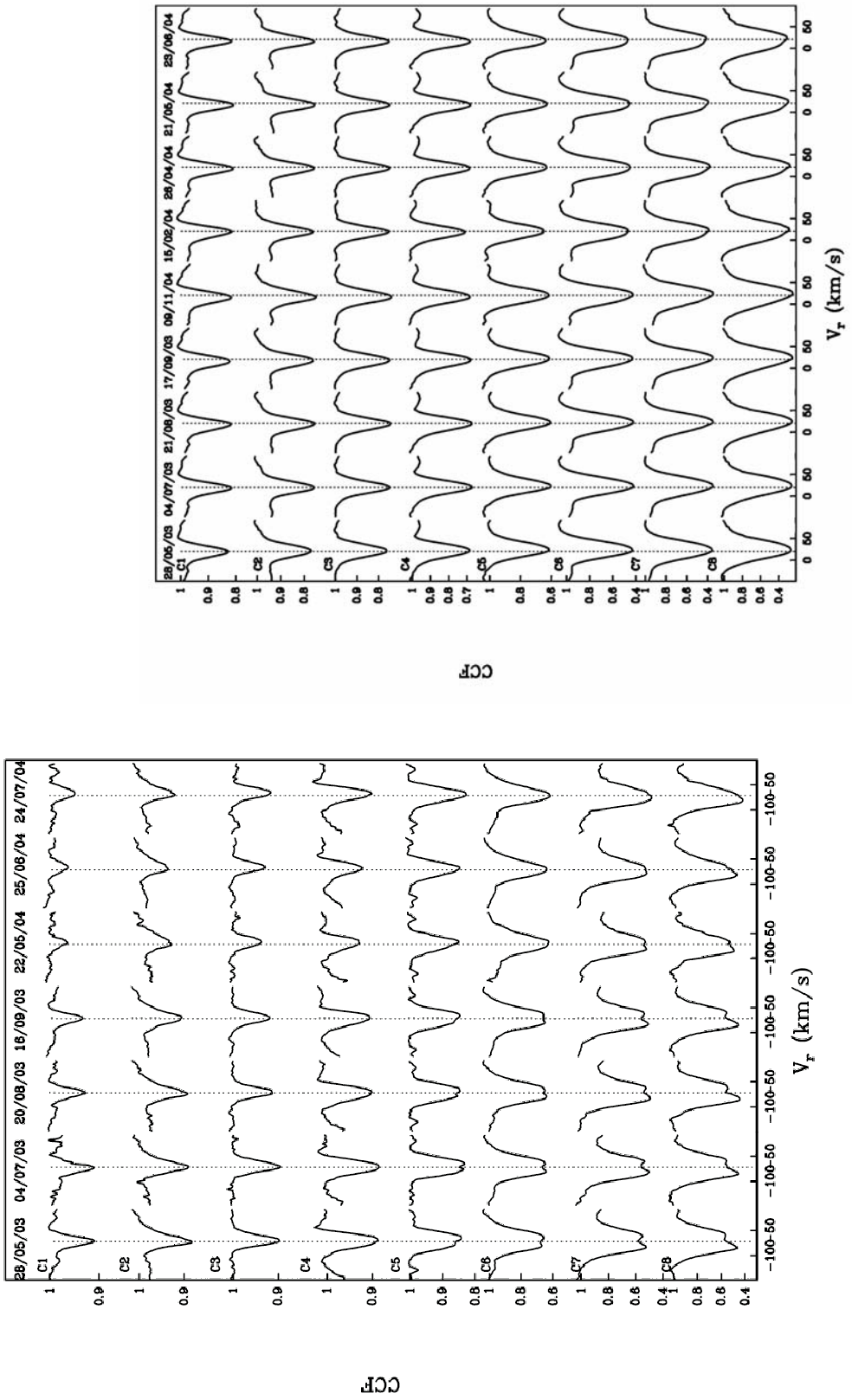

Figure 5.2: Observed Cross Correlation profiles. The innermost layer (probed by the C1 mask) is in the top row, and the outermost (mask C8) is presented at bottom row. The temporal sequence is indicated by the date at the top of every column. The central dashed line indicate the velocity measured in C1 at the first epoch. *Left panel:* SW Cep, the line doubling appear rather deep in the atmosphere and the outer layers have a broad and strong doubled line profile. *Right panel:* μ Cep, the variations are still visible but much smoother. Figures from Josselin & Plez (2007).

5.1.1 CCFs from the RHD simulations

I computed high resolution spectra (R=80000, v=3.7 km/s) in the region $4300 - 5300$ Å (corresponding to a one third of the range of the ELODIE spectrograph mounted on the 1.93m telescope at the OHP and used by Josselin & Plez 2007) for the best model available st35gm03n07 in Tab. 4.1. Its temperature is the closest to Betelgeuse effective temperature(3650K by Levesque et al. 2005), and it has a large number of runs. The resolution for the computation is enough to properly describe the CCF and to compare them with the observations where Josselin & Plez found that the uncertainty of cross correlation function is 1-2 km/s.
Fig. 5.3 and 5.4 display a small portion of the spectra computed for different snapshots with an enlargement on a spectral line of TiI at 4997.096 Å, $\log(gf)$=-2.118 and χ=0. eV (this line is include in mask C6). The total time covered is about 3.5 years and the spectra are about 70 days apart. Line profiles evolve with time: the differences (black line) between spectra for each snapshot and the average spectrum (red line) are not zero. In the Figure enlargements (right column), the black curve shows that some snapshots have the flux bigger in the red part of the line (>4997 Å) than the average spectrum and for some others snapshots the blue part (<4997 Å). See for example bottom right panel in Fig. 5.4.

The temporal fluctuations, over 3.5 years of simulation, at one σ with respect to the average value of the flux are $\sim 13\%$ for the whole spectral range (4300-5300 Å, Fig. 5.5).

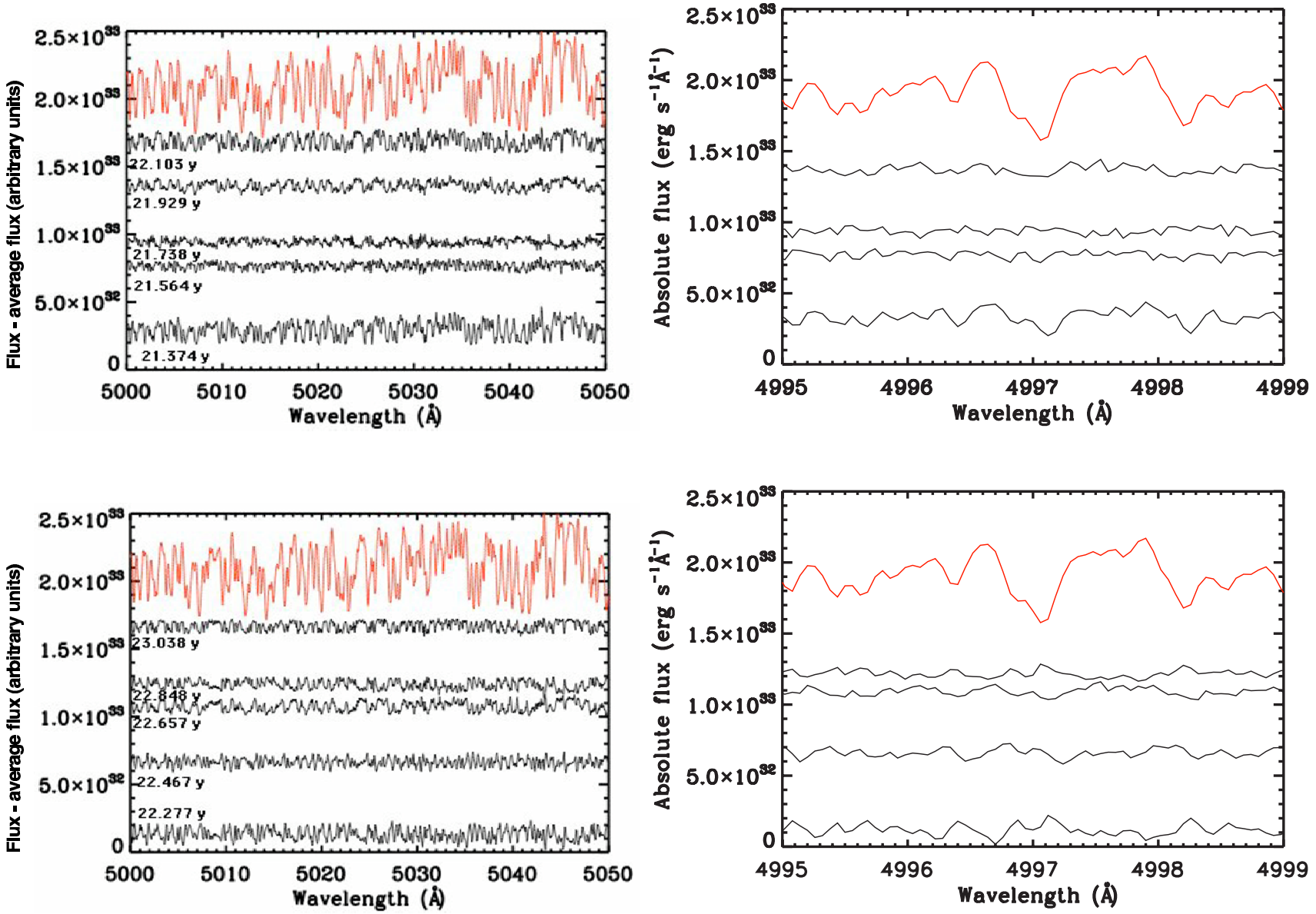

Figure 5.3: *Left column:* differences between spectra (black) and the average spectrum (red) computed from the best model st35gm03n07 in Tab. 4.1. The total time covered is about 3.5 years and the spectra are about 70 days apart. *Right column:* TiI line at 4997.096 Å, $\log(gf)$=-2.118 and χ=0. eV (this line is included in mask C6).

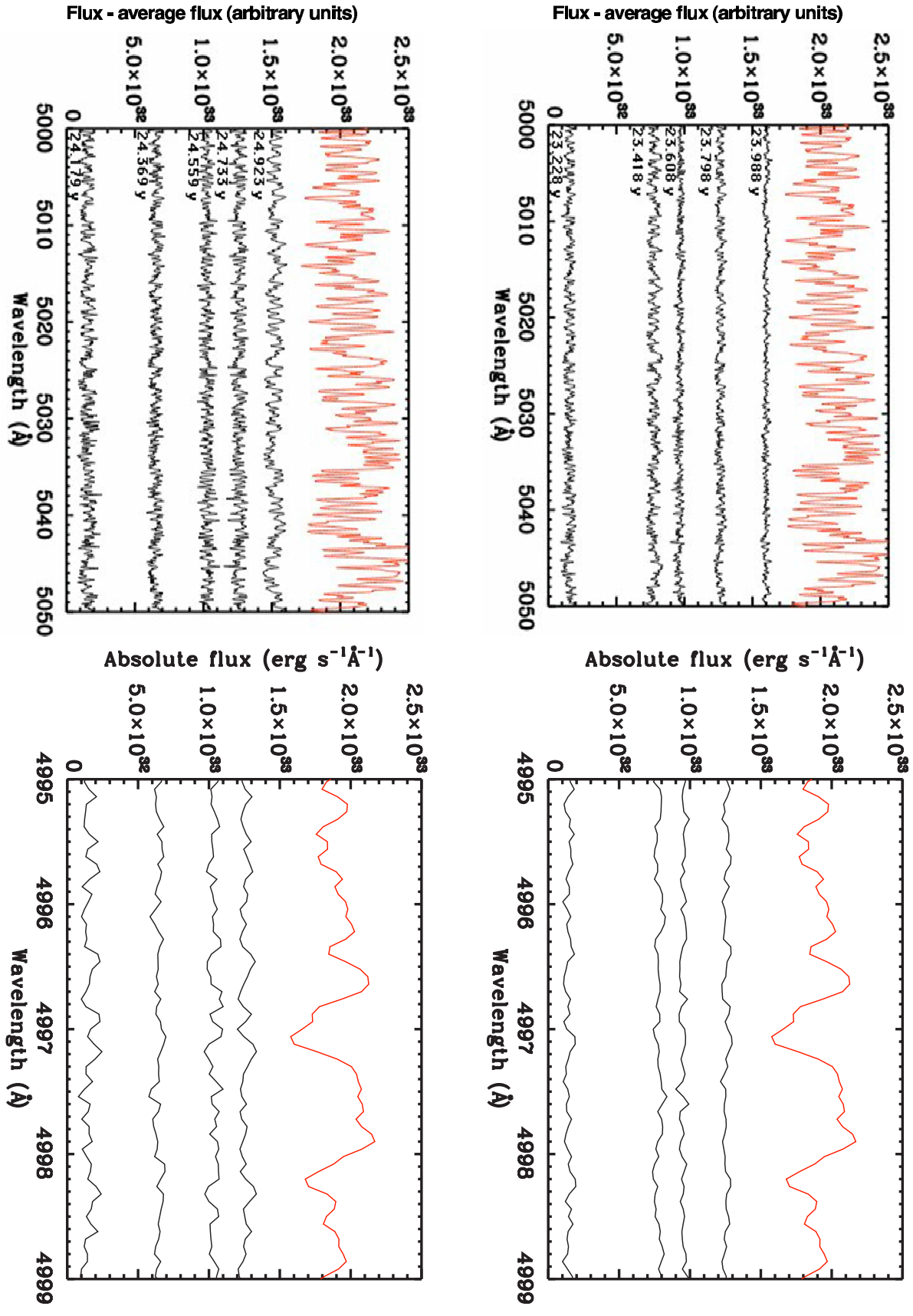

Figure 5.4: *Left column:* differences between spectra (black) and the average spectrum (red) computed from the best model st35gm03n07 in Tab. 4.1. The total time covered is about 3.5 years and the spectra are about 70 days apart. *Right column:* TiI line at 5020 Å, $\log(gf)$=-0.414 and χ=0.836 eV.

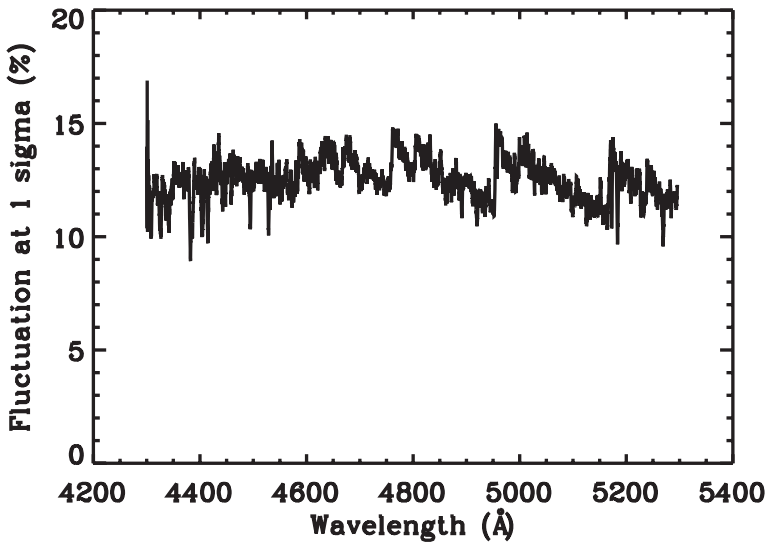

Figure 5.5: Calculated temporal fluctuations (one sigma) of the flux around its average value over 3.5 years of simulation (simulation st35gm03n07 in Tab. 4.1).

5.2 Determination of the characteristic velocity

I cross-correlated the calculated spectra with the masks built as described above. Fig. 5.6 displays an example of a temporal sequence of CCFs from RHD simulation st35gm03n07, and Fig. 5.7 is an enlargement of one time-step.

The CCFs (Fig. 5.6) present a wide variety of CCF shapes from one mask to another. As for observations, the asymmetries of the profiles increase as one progress from the mask C1 to the masks C5-C8. Mask C1 produces rather symmetric profiles.
In order to determine the characteristic velocities in the atmosphere, I have fitted one or two Gaussians or Lorentzians to the CCFs obtained from the temporal sequence of high resolution synthetic spectra. Some examples are shown in Fig. 5.8. The C1 CCF is most of the time adjusted with a single gaussian while the C7 and C8 CCFs are adjusted with two components (two Gaussian functions or one Gaussian and one Lorentzian) to reproduce the more complex profiles. In the intermediate masks (C2 to C6 CCFs), sometimes one single fit is enough and sometimes two components are necessary. The Gaussian and Lorentzian functions have been used half of the time equally, depending on the snapshot and masks.

The two velocities deduced from the correlation profiles computed from the mask C8 may be considered as indicators of the amplitude of the velocity dispersion in the corresponding line-forming regions. Following the notations used in Josselin & Plez (2007):

$$\delta v_{atm,i} = v_i\,(\mathrm{maskC8}) - v\,(\mathrm{maskC1}) \qquad i = 1, 2 \tag{5.1}$$

$$\delta v_{atm,3} = \delta v_2\,(\mathrm{maskC8}) - \delta v_1\,(\mathrm{maskC8}) \tag{5.2}$$

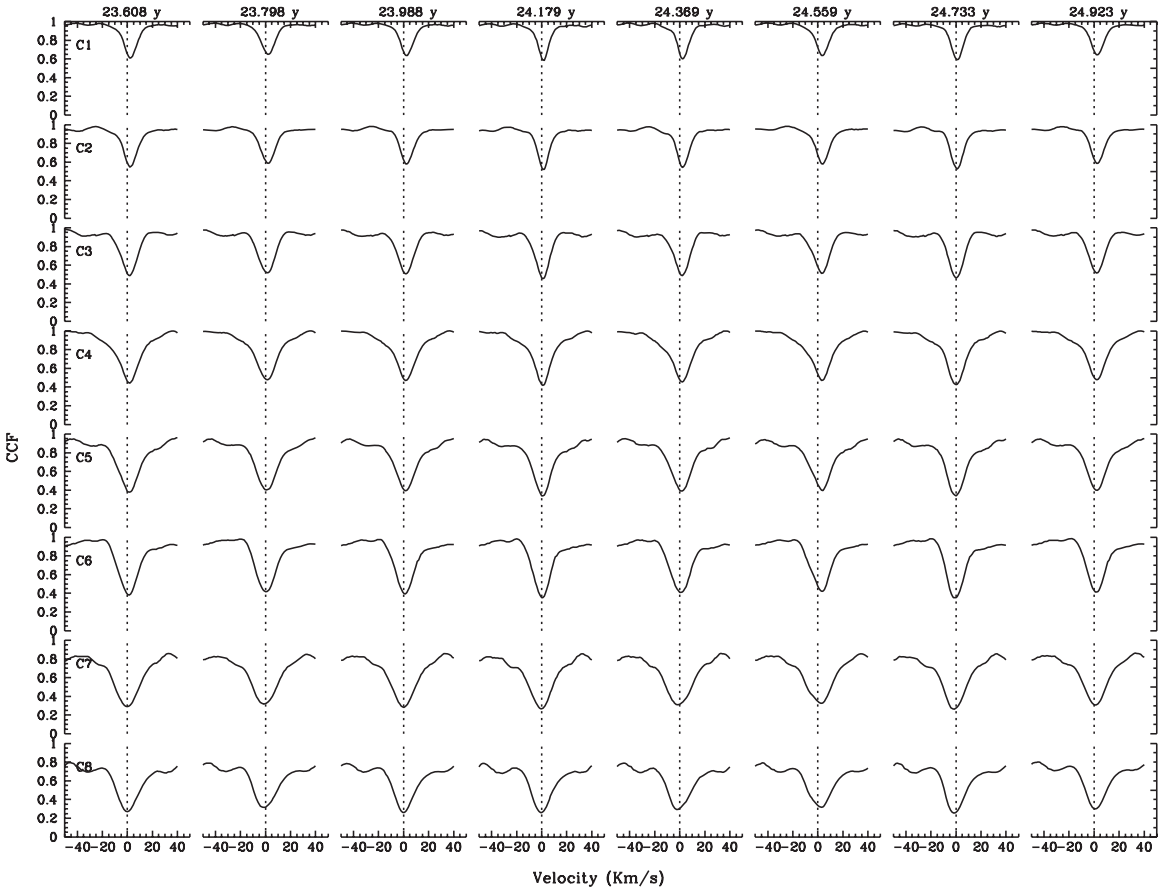

Figure 5.6: Temporal sequence of CCFs computed from the high resolution spectra in the range $4300 - 5300$ Å for the model st35gm03n07 (see Tab. 4.1). The mask are displayed as in Fig. 5.2. Dashed line is the zero velocity.

$v_{1,2}$ are the redshifted and blueshifted components measured in the mask C8. $\delta v_{atm,2}$ can be considered as indicative of the downward motions, $\delta v_{atm,1}$ as the upward motions and $\delta v_{atm,3}$ the convective velocity amplitude.

The temporal variations the velocities defined as above are reported in Fig. 5.9. δv_1 in bottom left panel, δv_2 in bottom right panel and δv_3 in top left panel. In this Figure, I have also reported the velocity in the Mask C1 as a function of the time. Mask C1 is shifted in average of 2.3 km/s over the temporal interval simulated (3.5 years). Thus, in the RHD simulation there is not a 0 km/s velocity but the convection affects also the lines that form farther deep in the atmosphere. This radial velocity correction may have to be applied to correct the observations.

The correlation profiles of the masks C5 to C8 present more or less remarkable asymmetries. The different components are determined with the fit functions. In mask C7 and C8 one component is systematically redshifted and the other one is blueshifted with respect to the mask C1. The CCF asymmetric profiles can be interpreted as: (i) a signature of the shock waves propagating in the atmosphere, (ii) non-gaussian chaotic movements.

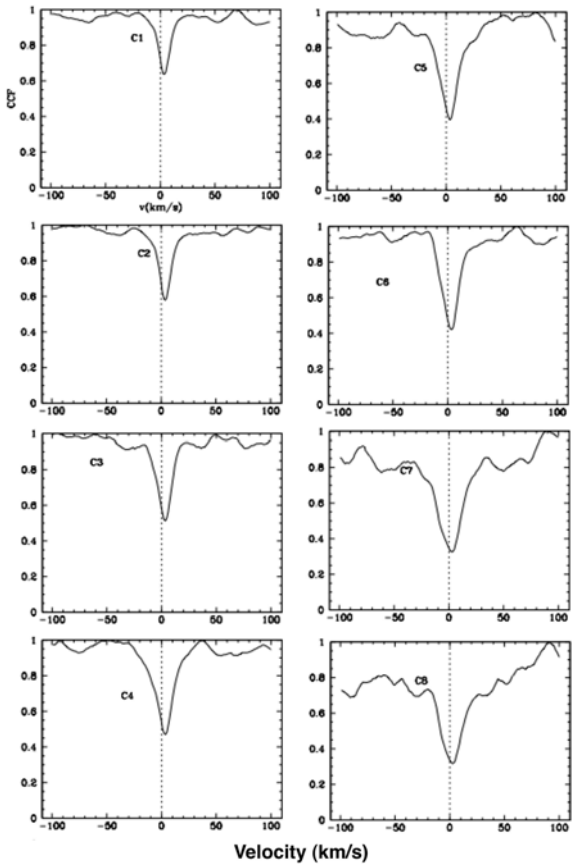

Figure 5.7: Enlargement of time-step 24.559 years from Fig. 5.6. Dashed line is the zero velocity.

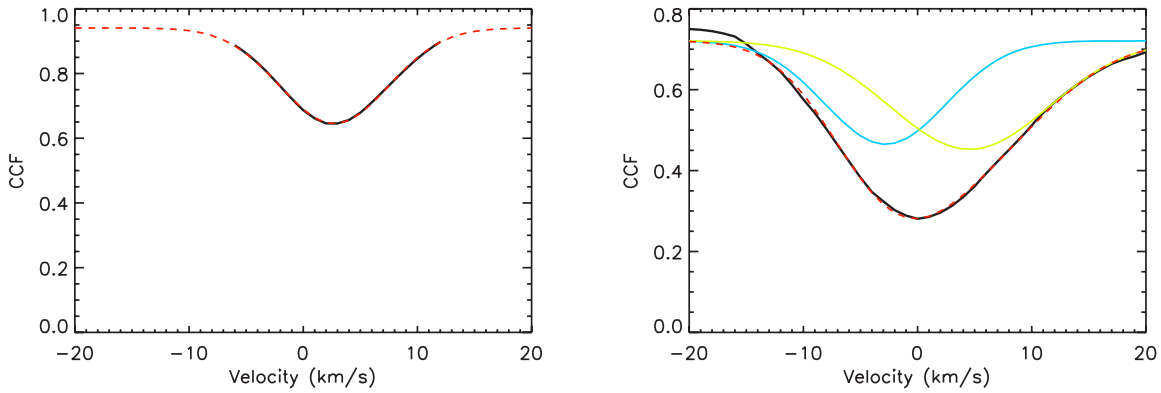

Figure 5.8: Correlation profile adjustment for the determination of the characteristic velocity. *Left panel*: Innermost mask C1 profile (black line) fitted with a single gaussian (red dashed line). *Right panel*: Outermost mask C8 profile (black) fitted with two gaussians (yellow and cyan), the final fit function (red dashed line) matches the CCF profile.

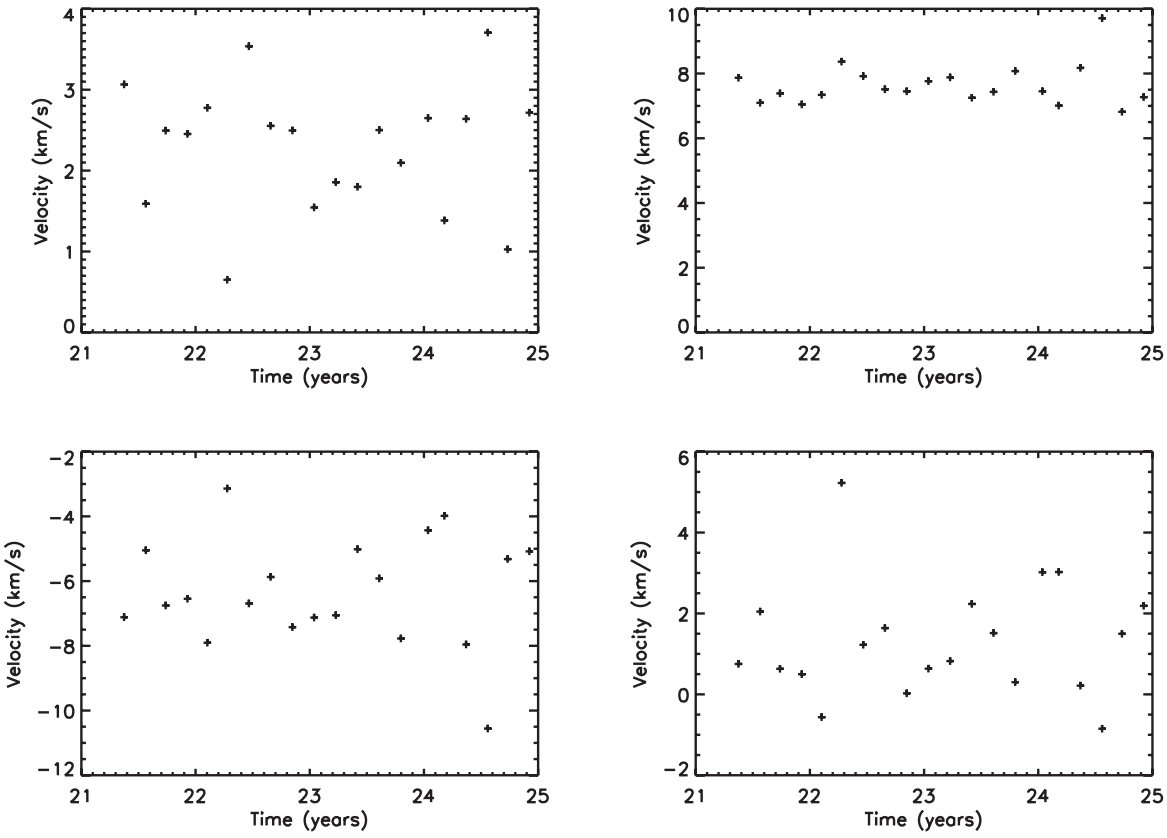

Figure 5.9: Temporal evolution of the Mask C1 velocity (top left panel); δv_1 (Eq. 5.1) in bottom left panel; δv_2 in bottom right panel; and δv_3 (Eq. 5.2) in top right panel. The total time simulated is 3.5 years.

I think that the first option is more plausible because the double CCF profile is not distributed randomly but there is a connection between masks of the same snapshot. For example, in the snapshot 151 in Fig. 5.7, a blue component in the CCF profile is already visible in mask C4 at -20 km/s; then the feature develops towards the C5 and C6 for eventually reach a clear signature of the line doubling in masks C7 and C8.

5.2.1 Results - velocities

Once measured the characteristic velocities, I can compare them to observation by Josselin & Plez (2007). Fig. 5.10 shows the velocity amplitudes as a function of the effective temperature.

The temporal average values (over 3.5 years) of the measured velocities with CCFs in the simulations are $< \delta v_{atm,1} >=$ -6.3 km/s, $< \delta v_{atm,2} >=$ +1.3 km/s and $< \delta v_{atm,3} >=$ 7.6 km/s. Their amplitudes ($\Delta_{atm,i}$=Maximum($\delta v_{atm,i}$)-Minimum($\delta v_{atm,i}$) are: 7.4 km/s for the $\Delta_{atm,1}$, 6.1 km/s for the $\Delta_{atm,2}$ and 2.9 km/s for the $\Delta_{atm,3}$.
The model atmospheric velocities measured with the CCFs have their amplitudes and

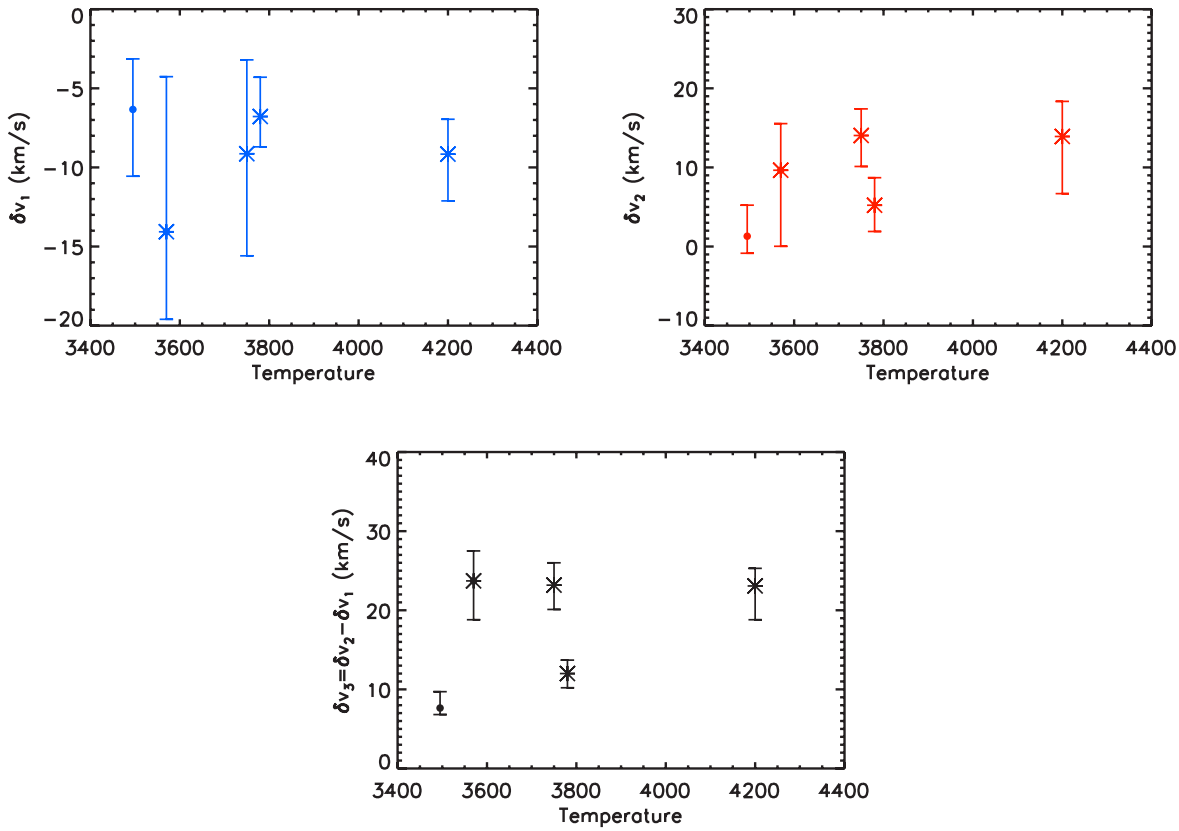

Figure 5.10: Velocity amplitude in the model (described in the text) as a function of the effective temperature compared to four observations by (Josselin & Plez 2007, SW Cep with 3570K, μ Cep with 3750K, ST Cep with 4200K, V466 Cas with 3780K). Top left panel shows the upward motions (δv_1 in Eq. 5.1); top right panel the downward motions (δv_2); and bottom panel the convective velocity amplitude (δv_3 in Eq. 5.2). The dots (model) and the stars (observations) are the average values over time. The observations used have the longest survey over the observed time (one year), while the time covered by the simulation is about 3.5 years.

average value over time always at the lower limit of the observations. The closet observed maximum amplitudes are those of V466 Cas where $\Delta_{atm,1}$=4.6 km/s, $\Delta_{atm,2}$=7.8 km/s and $\Delta_{atm,3}$=3.5 km/s.
Qualitatively, the observations show that stars with lower effective temperature (e.g., SW Cep with 3495K) have larger variations in the CCFs than the stars with higher effective temperature (V466 Cas with 3780K). See Fig. 5.2. The RHD simulation used has an effective temperature of 3495.2±14.3 K (Tab. 4.1) and it should show CCF variations and characteristic velocities similar to SW Cep; however, the simulation is much closer to V466 Cas.
In conclusion, the RHD simulation has velocity amplitudes in qualitative agreement with the observations. For this particular simulation, all the three velocity amplitudes are pretty similar to V466 Cas showing a coherent behavior of the velocity field with respect to the observations.

In addition, the reader must remember that there is an uncertainty on the effective temperature of the observed stars by Josselin & Plez. In fact, the T_{eff} is based on the $(V-K)$ color and using the polynomial fit for giant reported in (Bessell et al. 1998, Table 7). Levesque et al. (2006) showed that the effective temperatures derived with MARCS models fitting the optical spectrophotometry are systematically lower than those derived from the observed $(V-K)$. Thus, any conclusion about the temperature comparison between the RHD simulation and the observed stars is difficult.

The connection between the velocities measured with the CCFs and the velocities in the simulation is not trivial to find. One approach consists in using the velocities weighted with the contribution function to the line depression (Sect. 4.1) for some lines in the C1 and C8 masks. This work is in progress and it will presented in the near future.

5.2.2 Results - Correlations and velocity/depth/width diagrams

The relations between different velocity gradients defined as in Eq. 5.1 and 5.2 are displayed in Fig. 5.11 and 5.12. The results from the RHD simulation are directly compared to two observations in Josselin & Plez (2007). A clear correlation between $\delta v_{atm,2}$ (C8r-C1; which indicates the downward motions) and $\delta v_{atm,1}$ (upward motions) is visible in the simulation (top panel of Fig. 5.11) and in the observations (bottom panels). Note that the simulation velocity amplitude ($\Delta_{atm,1} = 6.1$ km/s and $\Delta_{atm,2} = 7.4$ km/s) is similar to μ Cep ($\Delta_{atm,1} \sim 12$ km/s and $\Delta_{atm,2} \sim 8$ km/s), while the velocity amplitudes of SW Cep are almost the double. Even if the velocity amplitudes are pretty similar, the absolute values of $\delta v_{atm,2}$ is ~ 10 km/s lower than μ Cep observation. Finally, the extreme snapshot at 22.103 years (red cross) and at 24.559 years (green cross) have negative velocities, that is not seen in the observations.

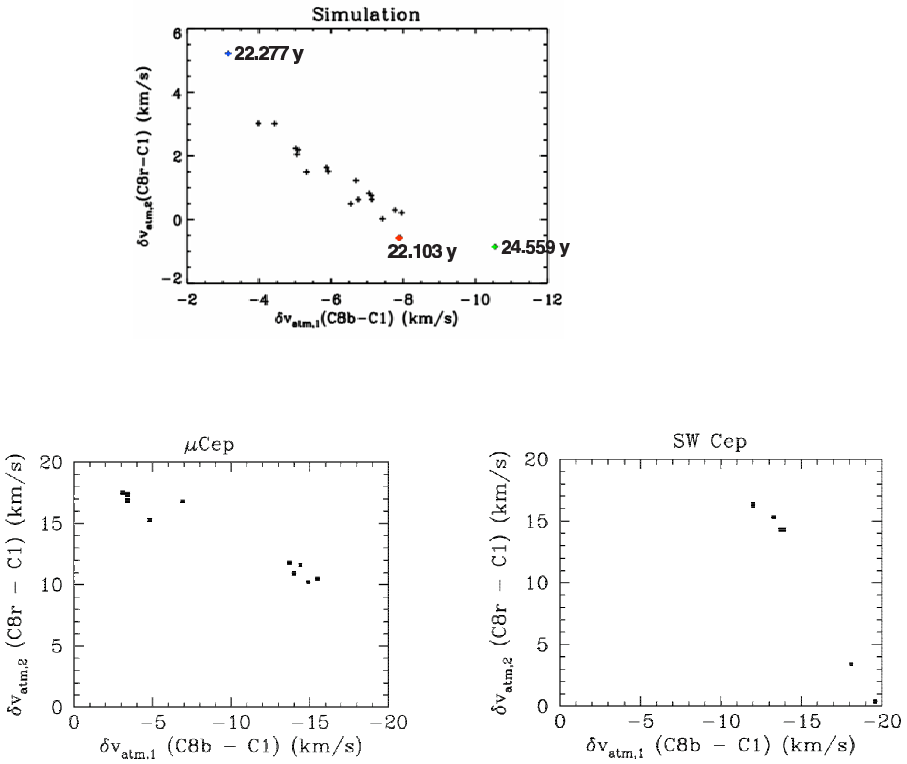

Figure 5.11: Relations between the $\delta v_{atm,1}$ and $\delta v_{atm,2}$ (see Eq. 5.1) for the RHD simulation (top panel) and two observed RSG by Josselin & Plez (2007) (bottom panels). Each point corresponds to one time-step or observation. C8r is the red component and C8b the blue component obtained in the CCF with the mask C8. For the simulation three snapshots are indicated with colored crosses.

There is no clear correlations between $\delta v_{atm,2}$ and $\delta v_{atm,3}$ (C8r-C8b; convective velocity amplitude) as reported in Fig. 5.12. SW Cep (bottom right panel) presents the same trend as in the simulation, while for μ Cep (bottom left panel) the situation is the opposite. In the observations the velocities are always positive, and in the simulation the measured velocities $\delta v_{atm,2}$ may also be negative (again the same extreme snapshots of Fig. 5.11).

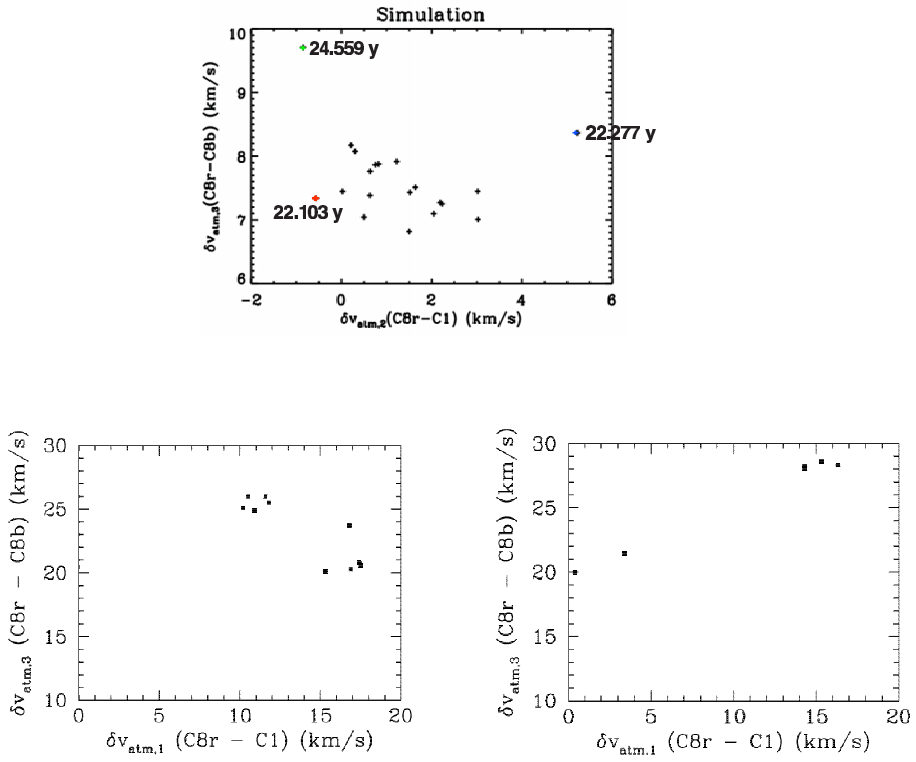

Figure 5.12: Relations between the $\delta v_{atm,2}$ and $\delta v_{atm,3}$ (see Eq. 5.1 and Eq. 5.2) for the RHD simulation (top panel) and two observed RSG by Josselin & Plez (2007) (bottom panels). Each point corresponds to one time-step or observations. C8r is the red component and C8b the blue component obtained in the CCF with the mask C8. Bottom left panel is μ Cep and bottom right panel is SW Cep. For the simulation three snapshots are indicated with colored crosses.

The snapshot at 24.559 years (green cross) and at 22.277 years (blue cross) have $\delta v_{atm,1}$ (upward motions) and $\delta v_{atm,2}$ (downward motions) really different (about 7 km/s) but $\delta v_{atm,3}$ not so different (1-2 km/s). The snapshot at 22.103 years (red) has $\delta v_{atm,2}$ really close to the snapshot at 24.559 years (green cross) while $\delta v_{atm,1}$ is about 2.5 km/s apart. I have tried to see what happens on the stellar surface, looking at the average velocity with the contribution function to the line depression (see Sect. 4.1). Fig. 5.13 shows the three snapshots. The large and central convective cell is visible in all the panels, the cell is moving to the right. Snapshot 22.103 years and 24.559 years appear

more similar in term of velocity magnitude: the redshifted velocity is more pronounced than in snapshot 22.277 years. This explains qualitatively the difference noticed in Fig. 5.11 and 5.12 between the extreme snapshots.

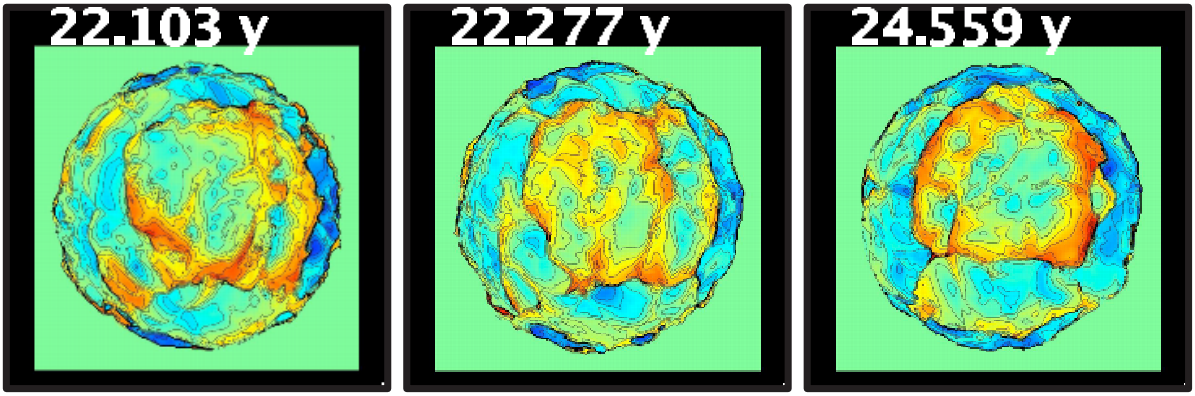

Figure 5.13: Velocity field weighted with the contribution function of the line depression (Sect. 4.1) for the three different snapshots. Colors follow usual radial convention from red (20 km/s) to blue (-20 km/s), green is zero. The contour black line is the contour plot of the velocity.

Josselin & Plez examined also the possible occurrence of correlations between the variations of each velocity. Some example with a good time coverage (about 1 year) are reported in Fig. 5.14 central and bottom row. They also reported the time variations in both depth and velocity for each component (some examples are shown in Fig. 5.15, central and bottom row). They conclude that there is no cyclic behavior in the observations, at least for the survey time.
In the same Figures, I have reported also the RHD simulation velocity-velocity diagram (Fig. 5.14 top row) and depth-velocity diagram (Fig. 5.15 top row). Left panel of each row shows the total time covered in the simulations (3.5 years), while the right panel displays only 1 year.
The trend of variation in the model is in qualitative agreement with the observations. For example, the black curve in Fig. 5.14 has similar slopes in the observations and in the simulation. For the latter, it is already visible in Fig. 5.11 and in the simulation the slope of the black curve is 1 (i.e., $\delta v_{atm,2}$ - $\delta v_{atm,1}$ = const., $\sim$ 8 km/s - Fig. 5.9 top right panel).
Nor the 3.5 years or the 1 year temporal coverage in the simulations show exactly the same curves of variations as in the observations and the RHD simulation seems to have more cyclical variations than the observations. The $\Delta =< \delta v_{atm,2} > - < \delta v_{atm,1} >$ between the downward motions (red curve) and upward motions (blue curve) is $\sim$20 to 25 km/s in the observations while in the simulation it is $\sim$8 km/s (see also Fig. 5.11, top panel)

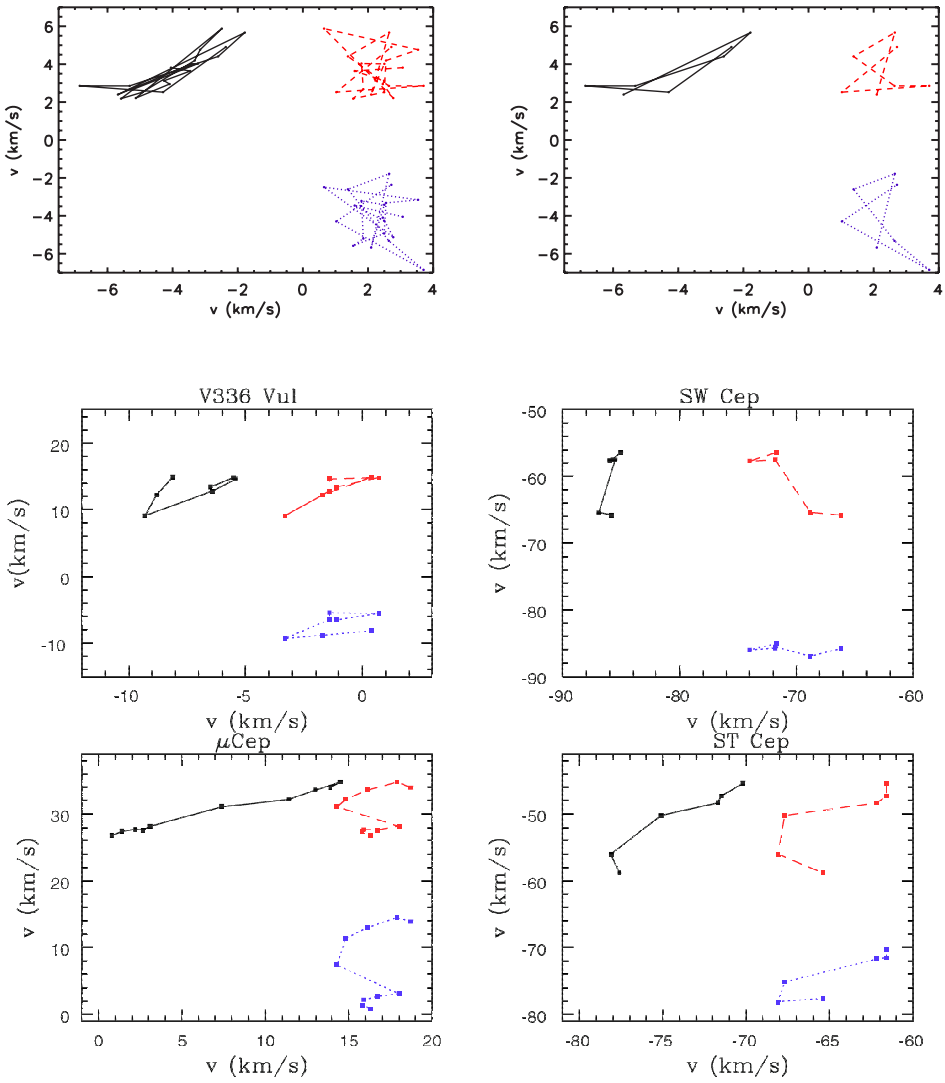

Figure 5.14: Velocity-velocity diagrams for the RHD simulation described in the text (top left panel for 3.5 years and top right for 1 year of simulation time covered) and for 4 RSG by Josselin & Plez (2007, Fig. 8) (central and bottom row). In each panel, the black curve is vC8r vs. vC8b (ordinate vs. abscissa), the red dashed curve vC8r vs. vC1 (downward motions), and the blue dotted curve vC8b vs. vC1 (upward motions).

Also the general trend of blue and red components of the velocities in Fig. 5.15 are in agreement between the model and the observations. In particular, the slopes and the amplitude of the velocities of the simulation are similar to μ Cep. There are two main difference between the CCF depths in the model and in the observations: (i) the depth of mask C1 (black line) in the model is bigger than what is observed; (ii) again, the Δ between the downward motions (red curve) and upward motions (blue curve) is $\sim$20 to 25 km/s while in the simulation is $\sim$8 km/s.

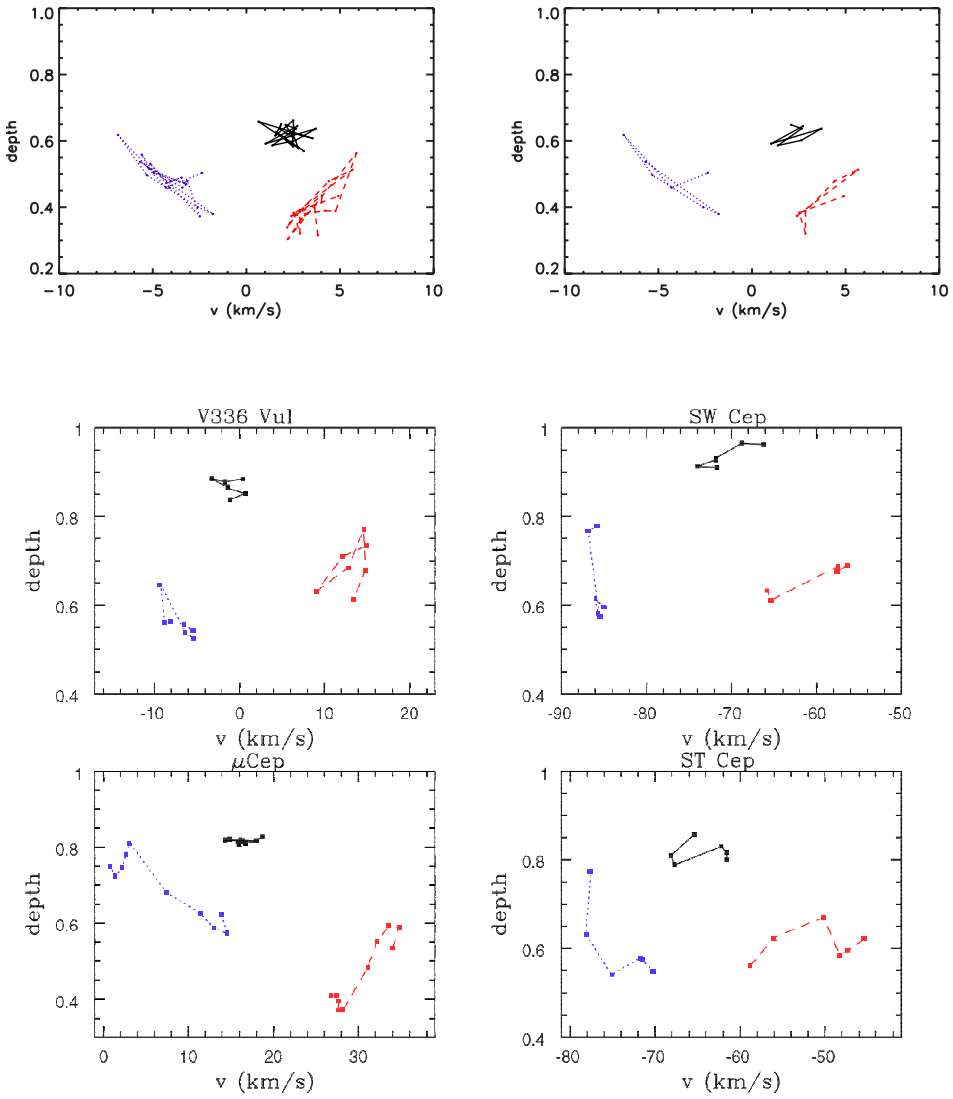

Figure 5.15: Depth as a function of velocities for the RHD simulation described in the text (top left panel for 3.5 years and top right for 1 year of simulation time covered) and for 4 RSG by Josselin & Plez (2007, Fig. 9) (central and bottom row). In each panel, the central black solid curve corresponds to the CCF obtained with mask C1, the left blue dotted and the right dashed curves belong to the CCF obtained with mask C8.

Fig. 5.16 shows the predicted width-velocity diagram, The colors have the same meaning as in previous Figures. The width measured from the CCFs is larger for the downward motions (red curve) than for the other two curves. This could signify that the downward motions broaden more the spectral lines that the upward motions (blue curve). This prediction must be compared with the observations (in progress).

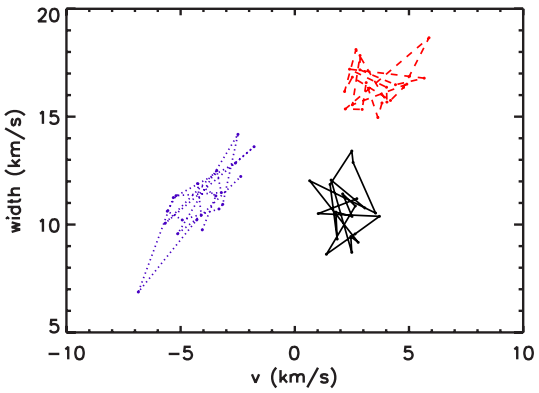

Figure 5.16: Width as a function of velocities for the RHD simulation described in the text (for 3.5 years of simulation time covered). The black solid curve corresponds to the width of mask C1, the blue dotted to the width of mask C8-blue component and the red dashed curves to width of mask C8-red component.

The velocity amplitudes in the simulation appear smaller than what is observed. The preliminary results indicate that the velocity field appears unchanged with respect to the increasing effective temperature (in the range 3300 K to 3500 K and same surface gravity) or resolution (from 235^3 to 315^3 grid points with similar effective temperature and surface gravity).
I think that the use of a more physically correct treatment of opacity in the RHD simulation could change the velocity amplitude in the RSG atmosphere. Non-grey treatment of opacities is expected to cause a closer coupling to the radiative equilibrium temperature stratification and strongly influences the evolution of the flow features (Ludwig et al. 1994 and Stein & Nordlund 1998). Convective overshoot could cool the higher photospheric layers ($\tau_{Rosseland} \lesssim 0.1$) and may change the dynamics of the atmosphere. I discuss this in Chapter 9.